City Research Online

City, University of London Institutional Repository

Citation: Stefanitsis, D., Koukouvinis, F., Nikolopoulos, N. & Gavaises, M. (2021). Numerical Investigation of the Aerodynamic Droplet Breakup at Mach Numbers Greater Than 1. Journal of Energy Engineering, 147(1), 04020077. doi: 10.1061/(asce)ey.1943-7897.0000720

This is the accepted version of the paper.

This version of the publication may differ from the final published version.

Permanent repository link: https://openaccess.city.ac.uk/id/eprint/24574/

Link to published version: https://doi.org/10.1061/(asce)ey.1943-7897.0000720

Copyright: City Research Online aims to make research outputs of City, University of London available to a wider audience. Copyright and Moral Rights remain with the author(s) and/or copyright holders. URLs from City Research Online may be freely distributed and linked to.

Reuse: Copies of full items can be used for personal research or study, educational, or not-for-profit purposes without prior permission or charge. Provided that the authors, title and full bibliographic details are credited, a hyperlink and/or URL is given for the original metadata page and the content is not changed in any way.

City Research Online: http://openaccess.city.ac.uk/ publications@city.ac.uk

Manuscript
Click here to access/download;Manuscript;Revised_Manuscript_final.docx

Numerical investigation of the aerodynamic droplet breakup at Mach numbers>1

Affiliations

Dionisis Stefanitsis[*1,], Phoevos Koukouvinis[2], Nikolaos Nikolopoulos[3], Manolis Gavaises[4]

[1]Research fellow at the Centre for Research and Technology Hellas/Chemical Process and Energy Resources Institute (CERTH/CPERI), Egialeias 52, Marousi, Greece. E-mail: stefanitsis@certh.gr

[2]Research fellow at the City University London, School of Engineering and Mathematical Sciences, Northampton Square, EC1V 0HB London, UK. E-mail: Foivos.Koukouvinis.1@city.ac.uk

[3]Researcher B at the Centre for Research and Technology Hellas/Chemical Process and Energy Resources Institute (CERTH/CPERI), Egialeias 52, Marousi, Greece. E-mail: n.nikolopoulos@certh.gr

[4]Proffesor at the City University London, School of Engineering and Mathematical Sciences, Northampton Square, EC1V 0HB London, UK. E-mail: M.Gavaises@city.ac.uk

Abstract

The present work examines numerically the breakup of water droplets exposed to gas flows at Mach numbers Ma>1, which resemble the ambient conditions encountered in the injection systems of scramjet (supersonic combustion ramjet) engines. A CFD model is utilized which solves the compressible Navier-Stokes equations, the energy equation, the mass conservation in volume fraction form (volume of fluid method) along with two equations of state to model the density variations of the two phases. In addition, a coupled VOF/Lagrange model is employed to capture the appearance of micro-droplets, which are smaller than the smallest grid cell. As a first step, a 2-dimensional planar simulation (water column) is performed at conditions of Ma=1.47 in order to validate the numerical model; its results are compared against published experimental and numerical data. Good agreement

is observed for the temporal evolution of droplet shape, the streamwise deformation, the leading-edge displacement as well as the shock wave reflection. Subsequently, the validated model is utilized to perform a 3-D simulation at Ma=1.23, which corresponds to the conditions of previous experimental studies, and its results are compared against the experimental data as well as the results from previous numerical studies, showing good agreement. Furthermore, surface instabilities are observed at the droplet surface initiated by interfacial instabilities due to the shearing effect and the interaction with the shock-wave, pertaining to Kelvin-Helmholtz and Rayleigh-Taylor instabilities, despite the stabilising contribution of surface tension; viscosity effects are found to play an insignificant role.

Keywords

Droplet breakup; shock wave; high Mach number; CFD; surface instabilities;

Introduction

The breakup of droplets exposed to Mach numbers >1 has received a lot of attention recently due to its application in supersonic combustion ramjet (scramjet) engines (Liu et al. 2018). These types of engines utilize the supersonic vehicle speed to compress the incoming airflow without the use of a compressor. Other non-dimensional numbers that are usually utilised for classifying the breakup of droplets are the Weber (We), Ohnesorge (Oh) and Reynolds (Re) numbers as well as the density (ε) and viscosity ratios (N) of the two phases (Guildenbecher et al. 2009); these are calculated based on the post-shock properties as:

$$We = \frac{\rho_g U_{sh}^2 D_0}{\sigma} \qquad Oh = \frac{\mu_L}{\sqrt{\rho_L \sigma \mathrm{D}_0}} \qquad Re = \frac{\rho_g U_{sh} D_0}{\mu_g} \qquad \varepsilon = \frac{\rho_L}{\rho_g} \qquad N = \frac{\mu_L}{\mu_g} \tag{1}$$

47 The breakup timescale can be also approximated by the non-dimensional correlation proposed by
48 (Nicholls and Ranger 1969) ($t^*=t/t_{shear}$):
49

$$t_{shear} = \frac{\mathrm{D}_0}{U_{sh}}\sqrt{\varepsilon} \quad (2)$$

50
51 Experimental studies on the breakup of droplets at high Ma numbers were performed as early as 1958,
52 when (Engel 1958) conducted experiments with water droplets exposed to an air flow of Mach number
53 ranging from 1.3 up to 1.7. She observed the formation of a mist at the periphery of the droplet and
54 also measured its breakup time. Later, Boiko and co-workers (Boiko et al. 1987; Boiko and Poplavski
55 2009) performed experiments with droplets of various liquids (water, alcohol, glycerine, and tridecane)
56 interacting with flows of Helium and air at Mach numbers ranging from 0.15 up to 4, and Weber
57 numbers greater than 400. They observed that the disintegration of the droplets originates from their
58 surface (core or periphery) and they attributed it to the appearance of Rayleigh-Taylor and Kelvin-
59 Helmholtz (KH) instabilities. The research group of K. Takayama (Wierzba and Takayama 1988; Yoshida
60 and Takayama 1990) examined experimentally the breakup of water droplets in an air flow of Ma
61 number ranging from 1.3 up to 1.56 and *We* number between 600 and 760. They divided the breakup
62 process into four stages: i) disruption of the liquid surface, ii) droplet deformation and initiation of the
63 formation of micro-droplets, iii) continuous stripping of micro-droplets until deformation reaches
64 maximum, and iv) remaining parent droplet breaks into large fragments. Joseph and co-workers
65 (Joseph et al. 2002; Joseph et al. 1999) examined experimentally the breakup of Newtonian and
66 viscoelastic droplets due to the interaction with a shock-wave of Mach number from 2 up to 3.03, We
67 number from 11700 up to 169000 and Oh number from 0.002 to 82.3. They encountered bag and bag-
68 and-stamen breakup modes even at such high We numbers, owing to the high Oh of the viscoelastic
69 liquids. Moreover, they developed a simplified theory to predict the critical wave length and growth
70 rate of the Rayleigh–Taylor (RT) instabilities.

Theofanous and co-workers (Theofanous and Li 2008; Theofanous et al. 2012) conducted experiments with water and viscous liquid droplets (silicon oil, glycerol and tri-butyl phosphate) suddenly exposed to supersonic gas streams. The examined Ma numbers ranged from 1.1 up to 3.5, the We numbers from 12 up to $2 \cdot 10^5$ and the Oh numbers from 0.0012 up to 540. They utilized the laser-induced fluorescence technique to visualize the droplets and questioned the results of the previous experiments, which used the shadowgraph method. Specifically, they attributed the breakup of the droplets at We numbers greater than 1000 to the shear induced entrainment (SIE) instead of the previously thought Rayleigh–Taylor piercing (RTP); they concluded that the latter occurs at We numbers in the range of 10 up to 100. In addition, they questioned the existence of the catastrophic breakup regime and stated that it is a mirage of the shadowgraph technique. Finally, they observed that Kelvin-Helmholtz instabilities play an important role in the breakup of viscous liquids. Later, (Yi et al. 2017) studied experimentally and numerically the early-stage deformation of water droplets in a supersonic air flow of Mach number ranging from 1.39 up to 1.90, and We number in the order of 10^3-10^4. They identified two mechanisms that are responsible for the droplet deformation at the early-stages, namely: i) pressure mechanism, which is responsible for the droplet flattening, and ii) shear mechanism, which is responsible for the formation of the small rings and bulges. Recently, (Hébert et al. 2019) studied experimentally and numerically in 2-dimensions, using an in-house code called Hesione, the breakup of water droplets exposed to gas flows of Ma=4.2-4.6 and We$>10^5$. They encountered the catastrophic breakup mode and divided the breakup process into three steps: i) droplet flattening, ii) fragmentation initiation at the outer rim of the droplet, and iii) droplet takes the shape of a filament aligned with the flow.

Turning now to the numerical studies of droplet breakup at high Ma numbers, (Surov 1995) was one of the first to study numerically the interaction of a shock wave with a liquid droplet. He investigated water and glycerine droplets at Ma numbers ranging from 3 to 10 and observed that an increase in liquid viscosity leads to a slight decrease in the rate of deformation of the droplet, while the liquid

density affects substantially the droplet deformation and displacement. Chang and co-workers (Chang et al. 2013; Liou et al. 2009) performed 2-D axisymmetric simulations using the AUSM+- numerical scheme (Chang and Liou 2007) of water and glycerol droplets exposed to an airflow of Ma number in the range of 0.29 up to 3, We number from 520 up to $5.4 \cdot 10^4$ and Oh number up to 1.9. They identified the RTP and SIE breakup modes and attributed each breakup mode to the Rayleigh–Taylor and Kelvin-Helmholtz instabilities, respectively, similar to the experimental studies of (Theofanous and Li 2008; Theofanous et al. 2012). (Xiao et al. 2017) used the coupled Level Set with Volume of Fluid (CLSVOF) interface tracking method to study the breakup of tributylphosphate droplets in supersonic flows. With a fixed Mach number equal to 3, they investigated the effect of density ratio, which ranges from 18,544 up to 667,577 and We number in the range of 15 to 75. They encountered the bag, bag-and-stamen and multimode breakup modes and concluded that the Weber numbers separating the different breakup modes, as well as the breakup initiation time, are higher in supersonic flows compared to those of the subsonic ones. (Guan et al. 2018) used the five equation model (Euler equations coupled with the stiffened gas equation of state (EoS)) to study the axisymmetric breakup of water, gelatine, fat and dodecane droplets subjected to an air shock-wave. They examined Ma numbers in the range of 1.39 up to 3.9 and We numbers of the order of 10^3; they observed that there is a saddle point (point of zero velocity) inside the droplet; its position was found to depend on the Ma number and proposed a simplified theory to predict it. (Meng and Colonius 2018; Meng 2016) also used the five-equation model of (Allaire et al. 2002) to simulate in 3-dimensions the breakup of a water droplet exposed to an air flow of Ma=1.47 and We=780. They compared qualitatively their results with those of the experimental study of (Theofanous et al. 2004); good agreement was found regarding the initial droplet deformation into a muffin-like shape, as well as the following disintegration into two liquid sheets, in agreement with (Liu and Reitz 1997). Moreover, KH instabilities were observed pertaining to the SIE breakup mode, which was also reported in (Theofanous et al. 2004). Nevertheless, the micro-mist appearing at the periphery of the droplet was not captured in that study. For the same conditions,

121 (Kaiser et al. 2017) used the Level Set (LS) method coupled with the compressible Euler equations and
122 the stiffened-gas EoS to simulate the breakup of a water droplet exposed to an air flow. They
123 performed 2-D (water column) and 3-D simulations and confirmed the results of (Meng and Colonius
124 2018; Meng 2016) for the existence of two liquid sheets during the breakup of the droplet, while they
125 also observed a third sheet upstream of the droplet; however, they stated that 3-D simulations with
126 higher resolution are necessary to confirm this observation. Finally, (Liu et al. 2018) also utilized the
127 five-equation model and performed 3-D simulations of water droplet breakup in an airflow of Ma
128 number in the range of 1.2 up to 1.8. They presented qualitative and quantitative results for the droplet
129 drift, velocity and acceleration and defined three stages of the breakup process in the SIE regime: i)
130 surface instability, ii) droplet flattening, and iii) entrainment from the liquid sheet.
131 The current work investigates the breakup of a water droplet exposed to a flow of Ma ranging from
132 1.23 up to 1.47 with the aim to capture for the first time in CFD simulations (to the author's best of
133 knowledge) the appearance of micro-droplets stripped from the parent droplet. A numerical model is
134 utilized which solves the compressible Navier-Stokes equations, the energy equation, the conservation
135 of the volume fraction (VOF method) along with two equations of state to model the density variations
136 of the two fluids. Furthermore, a coupled VOF/Lagrange model is employed to capture the appearance
137 of micro-droplets, which switches from VOF to Lagrange models when certain user-defined criteria are
138 met. 2-D planar and 3-D simulations are performed in the commercial software FLUENT v19.2 and
139 qualitative and quantitative results are presented and compared with published experimental and
140 numerical data.
141 The paper is structured as follows: in the following chapter the numerical model is presented, followed
142 by a chapter with the computational setup and examined conditions. Next, the results of the
143 simulations are presented regarding the model validation with the 2-D planar domain as well as the 3-
144 D simulation using the VOF/Lagrange model. In the last section of the paper the main conclusions of
145 the current work are presented.

Numerical model

Flow equations and volume of fluid (VOF) method

The CFD model for the aerodynamic breakup of droplets solves the mass and energy conservation equations as well as the Navier-Stokes equations coupled with the Volume of Fluid (VOF) methodology of (Hirt and Nichols 1981) for capturing the interface between liquid and gas.

A single continuity equation is solved for both phases (no mass sources are taken into consideration)

$$\frac{\partial \rho}{\partial t} + \nabla \cdot (\rho \vec{u}) = 0 \tag{3}$$

, as also a single momentum equation; the resulting velocity field is shared among the phases:

$$\frac{\partial (\rho \vec{u})}{\partial t} + \nabla \cdot (\rho \vec{u} \vec{u}) = -\nabla P + \nabla \cdot [\mu (\nabla \vec{u} + \nabla \vec{u}^T)] + \rho \vec{g} + \vec{F}_{vol} \tag{4}$$

The surface tension forces are included in the momentum equation by using the Continuum Surface Stress (CSS) model of (Lafaurie et al. 1994). In the CSS model the volumetric force is calculated as

$$\vec{F}_{vol} = \nabla \cdot \left[\sigma \left(|\vec{n}| I - \frac{\vec{n} \otimes \vec{n}}{|\vec{n}|} \right) \right], \vec{n} = \nabla \alpha \tag{5}$$

The volume fraction α is defined as:

$$a = \frac{Volume\ of\ liquid\ phase}{Total\ volume\ of\ the\ control\ volume} \quad (6)$$

164

165 , where the α-function is equal to:

166 • 1, for a point inside liquid phase.

167 • 0, for a point inside gas phase.

168 • 0<α<1, for a point inside the transitional area of the two phases, the interface.

169

170 The transport equation for the liquid volume fraction, since no mass sources are taken into

171 consideration, is

172

$$\frac{\partial \rho_L \alpha}{\partial t} + \nabla \cdot (\rho_L \alpha \vec{u}) = 0 \quad (7)$$

173

174 The values of the density ρ and viscosity μ are calculated using linear interpolation between the two

175 phases weighted with the volume fraction α:

176

$$\rho = \alpha \rho_L + (1 - a)\rho_g \quad (8)$$

177

$$\mu = \alpha \mu_L + (1 - a)\mu_g \quad (9)$$

178

179 The energy equation is given in eq. (10) for a flow without species and negligible viscous energy

180 dissipation; preliminary 2D simulations using the viscous heating option of FLUENT (viscous heating

181 terms in the energy equation are enabled) have shown that the droplet deformation as well as the

182 displacement experience negligible change when the viscous heating effect is taken into account.

183

$$\frac{\partial(\rho \mathrm{E})}{\partial t} + \nabla \cdot [\vec{u}(\rho E + P] = \nabla \cdot (k \nabla T) \tag{10}$$

184

185 , where the energy *E* is given by

186

$$E = h - \frac{P}{\rho} + \frac{v^2}{2} \tag{11}$$

187

188 , with the sensible enthalpy *h* calculated in its general form (Sonntag et al. 2008) by

189

$$h = \int_{T_{ref}}^{T} C_p dT + \int_{p_1}^{p_2} \left[v - T \left(\frac{\partial v}{\partial T} \right)_p \right] dp \tag{12}$$

190

191 , where the specific volume is $v = 1/\rho$. For the ideal gas (air or nitrogen in this work) the second term
192 of the right-hand-side of eq. (12) becomes equal to zero, while for an incompressible material it
193 becomes equal to $\frac{P - P_{ref}}{\rho}$. In the case of weakly compressible materials, such as liquids, exposed to the
194 pressure variations encountered here, the difference between incompressible and weakly
195 compressible (e.g. Tait EoS eq. (13)) calculation of liquid enthalpy are negligible; preliminary
196 calculations showed that the error is less than 1% for pressures up to 450 bar.

197

$$h = \int_{T_{ref}}^{T} C_p dT + \frac{B \cdot n \left(1 + \frac{P - P_{ref}}{B} \right)^{\frac{n-1}{n}} - B \cdot n}{(n-1)\rho_{ref}} \tag{13}$$

198

199 , where B is a parameter and *n* is a material exponent equal to *7.15* for water (Ivings et al. 1998).

200

Equations of state (EoS) and rest of fluid properties

For the cases with large density variations, such as those encountered at Mach numbers > 1, the density of each fluid is given as function of its temperature and pressure using an equation of state for each phase: i) for the gas phase the ideal gas law is utilized ($\rho = PMW_{gas}/RT$), while for the liquid phase the Tait EoS is used (eq. (14)):

$$\left(\frac{\rho}{\rho_0}\right)^n = \frac{K}{K_0} \tag{14}$$

, where K is the bulk modulus, which is a measure of the compressibility of a liquid; it is given in its general form by:

$$\mathrm{K} = -\mathrm{V}\frac{dP}{dV} \tag{15}$$

For the examined conditions of the current work ($T \approx 293.15$K and P ranges from 1.01325 bar up to ~2.8 bar - see section with the computational setup) the bulk modulus can be assumed to vary linearly with pressure (Gor et al. 2016): $K = K_0 + n\Delta p$, with $\Delta p = p - p_0$ and $n = 7.15$ for water (Ivings et al. 1998), with reference values as: P_o=101325 Pa, ρ_0=998.2 kg/m^3, $K_0 = 2.2 \cdot 10^9$ Pa (Menon 2014). It should be noted that for such small changes in the temperature (ΔT<1 K) and pressure (ΔP~1.8 bar) the density of water changes less than 1% and therefore not much difference is expected in the results with the use of constant density; however, this was not known a priori. For the same reason, the rest of fluid properties (surface tension, viscosity, heat capacity and thermal conductivity) are taken constant for the liquid water at the initial temperature of 293.15 K. Preliminary CFD simulations using variable properties for water based on (Lemmon 2013; Wagner and Pruß 2002) and the tabulated method of (Koukouvinis; et al. 2020) have shown that the droplet deformation in both axes changes less than 1%,

while the leading edge displacement is overestimated by a maximum of 10% at the final stages of the simulation with the constant properties approach, probably due to difference in the fluid viscosity. For the gas phase (air or nitrogen), which has large variations in the pressure and temperature, the heat capacity and thermal conductivity are taken as functions of temperature, using the polynomial functions of (Perry and Green 1999). Finally, the viscosity of gas is found using the Sutherland's law (Sutherland 1893).

VOF-to-DPM model

In the VOF-to-DPM model the liquid volume fraction of a cell is converted into Lagrangian particles (droplets), when certain user-specified criteria are met. In order to avoid spurious momentum sources, an equal volume of gas is created in the VOF solution to maintain the volume conservation. The criteria for transition from VOF to DPM in a cell are: i) the volume-equivalent sphere diameter should be within a specified range, which for this work is chosen between zero and the diameter of a particle that would occupy half the volume of an interface cell; this ensures that the stripping of micro-droplets will initiate from the droplet interface when it is close to its initial spherical shape (a lower number would not allow that since the domain has a wedge-like shape and the volume of the cells increases radially). However, this choice affects the size of the stripped particles, as discussed in sub-section "Description of fluid flow" of the 3-D simulation. The second criterion (ii) is that the asphericity should be below 0.5 (the value of zero corresponds to perfect spheres, while the higher it is the more the shape deviates from that of sphere); the higher the value of the asphericity the higher the number of cells that are elected for conversion (in (Bo Shen 2019) they found that a value of asphericity equal to 0.5 corresponded to 95% of the mass of the spray being converted into Lagrangian particles). After the particles-droplets have been created, their trajectory is tracked using the force balance on each of them separately, as given by eq. (16):

$$m_d \frac{d\vec{u}_d}{dt} = m_d \frac{\vec{u} - \vec{u}_d}{\tau_r} + m_d \frac{\vec{g}(\rho_d - \rho_g)}{\rho_d} + \vec{F} \quad (16)$$

248

249 The first term on the right-hand side is the term of the drag force, the second term is the gravity force,
250 which is negligible compared to the aerodynamic force, and the third one includes all other forces
251 (virtual mass, pressure gradient etc), which in the current work of high density ratio (ρ_d/ρ_g >>1) are
252 considered negligible. τ_r is the droplet relaxation time calculated by:

253

$$\tau_r = \frac{\rho_d d_d^2}{18\mu} \frac{24}{C_D Re} \quad (17)$$

254

255 , with Re being the relative Reynolds number given by:

256

$$\mathrm{Re} = \frac{\rho_d d_d |\vec{u}_d - \vec{u}|}{\mu} \quad (18)$$

257

258 and C_d the drag coefficient, calculated using the spherical drag law as:

259

$$\mathrm{C}_d = a_1 + \frac{a_2}{Re} + \frac{a_3}{Re} \quad (19)$$

260

261 , where the coefficients α_1, α_2 and α_3 are given in (Morsi and Alexander 1972).

262

263 Computational setup and examined conditions

264 2-D simulation of water column breakup (model validation)

The CFD model has been utilized and validated in previous works of the authors for a number of applications; among them are the free fall of a droplet (Malgarinos et al. 2015), the droplet impingement on a flat wall (Malgarinos et al. 2014) or a spherical particle (Malgarinos et al. 2016; Malgarinos et al. 2017; Malgarinos et al. 2017), the aerodynamic breakup of droplets and droplet clusters at low *Ma* numbers (G. Strotos 2015; Stefanitsis et al. 2017; Stefanitsis et al. 2017; Stefanitsis et al. 2018; Stefanitsis et al. 2019; Stefanitsis et al. 2018; Stefanitsis et al. 2019; Strotos et al. 2016; Strotos et al. 2016; Strotos et al. 2016) and the droplet evaporation (Strotos et al. 2016; Strotos et al. 2016; Strotos et al. 2016). In this work, its validation is extended to the case of droplet breakup at high *Ma* numbers. For this reason, a 2-D planar (column) simulation is performed in the computational domain of Figure 1. The shock wave is initialized as a step change in pressure, temperature and velocity (pink color in the figure), which are calculated based on the desired *Ma* number using a Riemann solver (Toro 1997). The liquid droplet (or column in 2 dimensions) is initially stagnant located at a distance equal to $1D_0$ from the shock wave, while the passage of the shock triggers its motion and deformation. The pressure outlet boundary condition at the top of the domain patches the value of the temperature and pressure of the neighbouring cell at the boundary, via a UDF, implying transmissive and partially reflective boundary. The computational mesh has increasing cell size in the Y-direction, therefore increasing the numerical diffusion when a wave moves towards the boundary, smoothing the gradients and minimising reflections, thus avoiding the need to move the top boundary at a very large distance. The pressure boundary condition at the right of the domain is non-reflecting, while the one on the left is not in order to avoid discontinuities in the velocity. The grid comprises of rectangular cells applied at two regions of the domain with different grid density (420000 cells in total): i) a rectangle of $8D_0$ length and $3D_0$ height with a resolution of 50 cells per radius (cpR), starting from the front of the shock wave and extending $7D_0$ downstream of the droplet, and, ii) the rest of the domain, in which the cell size increases gradually as the distance from the droplet increases, similar to (Meng and Colonius 2015). The pressure equation is spatially discretized using the body force weighted scheme, while for

290 the momentum equation the second order upwind scheme (Barth and Jespersen 1989) is utilized. The
291 temporal discretization of all equations is done with the first order implicit scheme, while the time step
292 is such that the acoustic Courant number is equal to 0.8, i.e. below 1, which is common for flows with
293 shock waves (Koukouvinis et al. 2016; Meng and Colonius 2015). Moreover, the VOF equation is solved
294 implicitly and is spatially discretized using an equal blending between first and second order schemes,
295 which gives the best agreement with the results of (Igra and Takayama 2001; Meng and Colonius 2015).
296 The liquid droplet is water with diameter based on (Meng and Colonius 2015), while the surrounding
297 gas is air. The properties of both have been described in equations section and the resulting non-
298 dimensional numbers are presented in Table 1, calculated based on the post-shock properties. In the
299 following sub-sections, the results of the simulation are compared with the experimental data of (Igra
300 and Takayama 2001; Igra and Takayama 2001) and the simulation of (Meng and Colonius 2015).
301
302 **3-D simulation of water droplet breakup**
303 Apart from the well-known 3-D flow features appearing in the aerodynamic breakup of droplets, such
304 as surface instabilities, vortex shedding and formation of liquid sheets (Kaiser et al. 2017; Liu et al.
305 2018; Meng and Colonius 2018), a 3-D simulation is necessary in order to apply the VOF-to-DPM model,
306 which tracks the particles in 3-dimensions following the Lagrangian approach Figure 2 illustrates the
307 3-D computational domain that is utilized for the simulation of droplet breakup at high Ma number.
308 Similar to the domain used in the 2-D simulation (Figure 1), at the top and right boundaries of the
309 computational domain, pressure outlet boundary conditions are applied; while at its left boundary a
310 pressure inlet is assigned. Only 1/8 of the droplet is simulated (45^o), while periodic boundary conditions
311 are applied at the front and back of the computational domain. The choice of solving the 1/8 of the
312 droplet using periodic boundary conditions has been made in order to reduce as much as possible the
313 computational resources to make it possible to simulate the examined case with the current numerical
314 tools. Regarding the effect of this choice on the results, limitations of assuming symmetry of the flow

315 field appear in the deformation and breakup of droplets due to turbulence and vortex shedding;
316 nevertheless, these limitations do not affect much the shape of the main droplet (Jain et al. 2018; Liang
317 2016; Stefanitsis et al. 2017). However, as it has been observed in the experiments of (Achenbach
318 1974; Sakamoto and Haniu 1990) and the simulations of (Stefanitsis et al. 2017) vortices in flows
319 around spherical shapes detach periodically from a point at the wake of the droplet that rotates
320 periodically at 45^o around an axis that passes through the centre of the sphere; this can possibly affect
321 the trajectory and timing of detachment of the micro-droplets, something that requires the solution
322 of half the droplet in order to fully resolve it. The shock wave is initialized as a step change in the
323 temperature and pressure located at a distance of $1D_0$ from the centre of the droplet. In order to
324 introduce some necessary randomness in the process, the field is initialized with a small "random"
325 instantaneous velocity ($<1/100U_{sh}$), which is calculated based on the turbulent kinetic energy
326 estimated from the κ-ε model. The grid cells have a wedge like shape (similar to that of the domain)
327 and it has been created using the 2-D grid of the previous section revolved around the X axis (36
328 partitions in total); this gives a resolution at the interface close to 50cpR. The convective Courant
329 number is equal to 0.5, while the acoustic is 7.85; preliminary 2-D runs have shown that the temporal
330 evolution of droplet shape and velocity do not change much when a smaller time step is used
331 ($Cou_{acoustic}<1$), therefore saving a lot of computational time in the current 3-D simulation. The spatial
332 discretization of the VOF equation is done using the geo-reconstruct scheme (sharp interface) in
333 contrast to the more diffusive schemes used in the simulation of water column, due to restrictions of
334 the VOF-to-DPM model of FLUENT; the rest of the discretization schemes are the same as in the 2D
335 case.
336 The liquid droplet is water, while the surrounding gas is nitrogen, instead of air in the 2-D case, with
337 properties calculated as described in the sub-section "2-D simulation of water column breakup (model
338 validation)"; the diameter of the droplet is based on (Theofanous et al. 2012). The resulting non-
339 dimensional numbers are calculated based on the post-shock properties and are presented in Table 2.

Results and discussion

2-D simulation of water column breakup (model validation)

Description of fluid flow

In the numerical simulations of multiphase flows with shock waves, schlieren is commonly used for visualization of the process (Quirk and Karni 1996). The schlieren function is utilized to visualize the density variations of the flow field and is calculated, using eq. (20), as the exponential of the negative, normalized density gradient:

$$\varphi = \exp\left(-k\frac{|\nabla\rho|}{max|\nabla\rho|}\right) \quad (20)$$

, where k is a scaling parameter equal to 40 for air and 400 for water (Johnsen 2008).

The pressure and schlieren contours, as predicted by the simulation, are presented in Figure 3 for various time instances. At the time instance of t^*=0, the shock wave front touches the surface of the water droplet, while at t^*=0.017 it passes over it and part of it is reflected radially. The droplet starts to deform after some time from the pass of the shockwave, at approximately t^*=0.171, taking initially a mushroom-like shape (t^*=0.444) and followed by a deformed disk-like shape (t^*=0.808). Eventually the breakup occurs with liquid stripping from the periphery of the droplet, which is not clearly visible due to the diffusion of the volume fraction, attributed to the selection of the lower order discretization scheme. This scheme, however, gives results closer to those of (Igra and Takayama 2001; Igra and Takayama 2001; Meng and Colonius 2015).

Figure 4 presents the holographic interferograms from the experiment of (Igra and Takayama 2001) as well as the schlieren contours as predicted by the simulation of the current work along with that of (Meng and Colonius 2015), for two time instances. As it is observed from the figure, the shock wave

reflection is very similar in the three works for both time instances. The curved black lines correspond to the reflection (R) of the shock-wave in the droplet as well as its diffraction (D). Finally, it should be noted that the time in the experiments is higher compared to both simulations, probably due to a reporting error in (Igra and Takayama 2001) or a misunderstanding of the phrase "time after the interaction between the incident shock wave and the water column" of the original work of (Igra and Takayama 2001), as already discussed thoroughly in (Meng and Colonius 2015).

Results on droplet quantities

Figure 5 presents the temporal evolution of the non-dimensional streamwise and cross-stream deformation, as well as the leading-edge displacement of the droplet, as predicted by the experiment of (Igra and Takayama 2001), the simulation of (Meng and Colonius 2015) and the simulation of the current work (α=0.5). As the droplet deforms into an ellipsoid shape, the streamwise deformation gradually decreases with time, while the cross-stream one increases. The leading-edge displacement increases as the droplet moves in the streamwise direction. There is a good agreement between the results of both simulations and the experiment for the streamwise deformation and leading-edge displacement, while a discrepancy is observed with the experiments for the cross-stream deformation; however, the results of the two simulations are close.

3-D simulation of water droplet breakup

Description of fluid flow

Figure 6 illustrates the temporal evolution of droplet deformation as predicted by the experiment of (Theofanous et al. 2012), the simulation of (Meng and Colonius 2018) and the simulation of the current work. It should be noted that the conditions of this work and those of the experiment are identical, while in the simulation of (Meng and Colonius 2018), the Ma is equal to 1.47 instead of 1.23. Also, the shape in the simulation of (Meng and Colonius 2018) corresponds to the VOF iso-value of 0.01, while in the current work the iso-value of 0.5 is presented. The exact time of the experimental images is not

known since they originate from a video, while the time instances of the simulations have been chosen such as to best match the images of the experiments.

Similar to the 2-D simulations, the droplet initially deforms into a mushroom-like shape (t^*=0.274 and t^*=0.314 in the simulation of this work), followed by a disk-like shape (t^*=0.634). However, their main difference lies in the breakup initiation time, which is much faster for the 3-D simulation, since mirco-droplets are stripped from its periphery as early as t^*=0.274. This is attributed to the high velocities at the periphery of the droplet, as shown in Figure 7, which presents in the X-Y plane (Z=0) the contour of non-dimensional pressure ($P^*=P/P_{sh}$) at different time instances. The maximum value of the velocity is equal to 1.5, in agreement with the potential flow theory and the simulation of (Meng and Colonius 2018). The liquid stripping continues until a large part of the parent droplet has been converted into micro-mist (t^*=0.634), something that is also visible in the experiment of (Theofanous et al. 2012). The diameter of these micro-droplets ranges from approximately 25 μm up to 52 μm, which corresponds to the volume equivalent droplet diameter of an interface cell, and it is an input for the model. Nevertheless, in the simulation micro-droplets appear also at the core of the droplet, owing to a conical protuberance appearing axially at the leading edge of the droplet at t^*=0.234 and remaining up to t^*=0.634, as shown in Figure 8, which presents an enlarged image of the time instance t^*=0.314. The latter is attributed to the waves that appear at the surface of the droplet, due to the interaction with the shock wave, as shown in the dimensionless pressure $P^*=P/P_{sh}$ contour of Figure 7: at the time instance of t^*=0.234, the pressure is higher at the outer part of the droplet compared to its core, which is the case for the rest of the images, therefore creating the aforementioned protuberance. This is also present in the experiments, starting from the image corresponding to t^*=0.314 simulation time and being more visible at t^*=0.634, but to a smaller extent. Finally, “wrinkles” appear at the surface of the droplet visible in the simulation at time instance of t^*=0.234, which are also present in the experiments, but to a smaller extent.

To further understand the procedural deformation and disintegration of the droplet due to the accumulation of interfacial instabilities, as presented in Figure 6 and Figure 7, an analysis and explanation of the mechanisms of the droplet break-up is presented in the following section, examining the sources of vorticity generation on a 3-D slice of the geometry depicted in the previous section. In particular, the vorticity evolution equation can be expressed as (Green 1995):

$$\frac{d\boldsymbol{\omega}}{dt} = (\boldsymbol{\omega} \cdot \nabla)\mathbf{u} - \boldsymbol{\omega}(\nabla \cdot \mathbf{u}) + \frac{1}{\rho^2}\nabla\rho \times \nabla p + \nabla \times \left(\frac{\nabla \cdot \tau}{\rho}\right) + \nabla \times F_\sigma \tag{21}$$

The first term in the right-hand side represents vortex stretching/tilting, the second term represents vortex dilation, the third term represents the baroclinic torque, the fourth term expresses vortex diffusion due to viscous stresses, as defined in eq. 4 and the last term expresses the influence of body forces. Vortex stretching or tilting is due to the effect of velocity gradient on vorticity; it is a crucial mechanism in the generation of complex vortical structures and is considered responsible for the kinetic energy cascade process in turbulence (Wu et al. 2015). Vortex dilation is due to the volumetric expansion/contraction (the velocity divergence), which describes how fluid compressibility affects the vorticity. The baroclinic torque occurs due to the different alignment of density and pressure gradients and is responsible for the formation of Rayleigh-Taylor instabilities. The last term in the present simulation is only due to the influence of surface tension. Interestingly, as will be shown later, despite the high Weber number, influence of surface tension is non-negligible, although it contributes to stabilise the interface.

In Figure 9 a comparison of the strength of different factors affecting vorticity evolution is shown, on a z-slice, similar to the views used in Figure 7, showing the cross-section of the droplet. As observed from the values of the terms involved, viscous stresses have the lowest contribution in vorticity, being at least one order of magnitude lower than the other terms. Next, is the contribution of baroclinic torque, which is entirely located at the near interface region, mainly at the gas side due to the influence

435 of lower gas density in the baroclinic term. The strongest terms are due to manifestation of
436 compressibility effects (vortex dilation), the turbulent cascade (vortex stretching/tilting) and surface
437 tension, all terms having a similar order of magnitude. Indeed, based on a similar analysis by (Zandian
438 et al. 2018), surface tension effect on vorticity scales as $\sigma\kappa/\rho\Delta^2$, which is in the order of 10^{11} s^{-2} for
439 the present case, assuming a max. curvature of κ=10^6 m^{-1}, density in the order of 10^3 and mesh sizing
440 of ~25μm.
441 An important outcome of this analysis is that viscosity plays a marginal role in the development of the
442 droplet break-up; indeed, inviscid simulations also confirm this observation (not show in the present
443 work). Hence, the phenomenon is practically entirely interfacial driven, due to combined Kelvin-
444 Helmholtz, similar to (Theofanous et al. 2012), and Rayleigh-Taylor instabilities. Another observation
445 is that, despite the droplet We is ~1000, surface tension will have an effect in stabilising locally
446 interfacial instabilities, although the destabilising influence of the other terms is much stronger,
447 contributing to the disintegration of the droplet.
448 **Results on droplet quantities**
449 Figure 10 illustrates the temporal evolution of the dimensionless droplet velocity, displacement and
450 acceleration, as well as the unsteady drag coefficient, as calculated in the current work and in the
451 simulation of (Meng and Colonius 2018). The unsteady drag coefficient is calculated using the
452 momentum balance on the droplet and is given in equation (22). The droplet frontal area is calculated
453 by assuming a circular area based on the droplet's deformed diameter D_{cr} (assumed equal to D_z),
454 similar to (Meng and Colonius 2018).
455

$$C_d(t) = \frac{\frac{4}{3} D_0 \varepsilon \frac{\mathrm{d}U_d(t)}{dt} \frac{A_f(0)}{A_f(t)}}{\left(U_{sh} - U_d(t)\right)^2} \tag{22}$$

456

Both the velocity and the displacement of the droplet increase with an exponential fashion as the shock wave and the gas flow behind it crosses the droplet and forces it to move. The droplet acceleration starts from zero value, since the droplet is initially stagnant, while it increases rapidly due to the droplet being in motion from stagnation; after a small fluctuation at the initial stages of the simulation owing to the unsteady flow field, it eventually increases gradually as the droplet accelerates steadily. The drag coefficient experiences a similar decline at the initial stages of the simulation; however, it increases only slightly followed by a decrease at the later stages of the simulation. This is attributed to the increase of the frontal area of the droplet ($A_f(t)/A_f(0)$) as it deforms in the cross-stream direction. The results from the simulation of (Meng and Colonius 2018) follow a similar trend, while being slightly higher compared to the simulations of this study, probably due to the higher Ma number (1.47 compared to 1.23).

Finally, the temporal evolution of droplet deformation in both axes (streamwise and cross-stream) and surface area are presented in Figure 11. The cross-stream deformation and surface area increase as the droplet takes an ellipsoid shape, while the streamwise deformation decreases followed by a slight increase at the final stages of the simulation; this is attributed to the liquid sheets formed at the periphery of the droplet (Figure 6 at t*=0.634), which are also reported in the works of (Kaiser et al. 2017; Meng and Colonius 2018). The fluctuation in the value of cross-stream deformation at the time instance of approximately 0.5 is attributed to the stripping of the micro-droplets from its periphery, something that results in the decrease of the size of the parent droplet.

Conclusions

In the current work 2-D planar (column) and 3-D simulations were performed for droplets exposed to gas flows of Ma numbers ranging from 1.23 up to 1.46. The CFD model solves the compressible Navier-Stokes equations, the energy equation, the VOF equation along with two equations of state to model the density variations of the two phases. In addition, in the 3-D simulation the VOF-to-DPM model of

FLUENT was utilized, which switches from VOF to DPM when certain user-defined criteria are met, in order to capture the appearance of micro-droplets detached from the parent droplet.

The results of the 2-D simulation are compared against published experimental (Igra and Takayama 2001) and numerical (Meng and Colonius 2015) data and good qualitative agreement is observed for the pressure and numerical schlieren contours. In addition, the quantitative results for the streamwise deformation and the leading-edge displacement are also in good agreement with experiments. However, a discrepancy was observed for the cross-stream deformation.

Regarding the 3-D simulation, the predicted temporal evolution of droplet shape was similar to that of the experiments of (Theofanous et al. 2012). The simulation predicted the appearance of micro-droplets at the periphery of the droplet as well as surface instabilities (K-H and R-T) similar to the experiments. Finally, results for the droplet deformation and surface area were presented and a steady increase in the surface area and cross-stream deformation was observed, as the drop takes an ellipsoid shape, while the streamwise deformation initially decreases followed by an increase at the later stages of the simulations, due to the formation of liquid sheets at the periphery of the droplet.

Data availability statement

All data, models, or code that support the findings of this study are available from the corresponding author upon reasonable request.

Acknowledgements

Financial support from the MSCA-ITN-ETN of the European Union's H2020 programme, under REA grant agreement n. 675676 is acknowledged.

Notation

Roman symbols

A_f	Frontal area [m^2]
c	Speed of sound [m/s]
C_d	Drag coefficient [-]
Cou	Courant number [-]
C_P	Specific heat [J/kgK]
D	Droplet diameter or deformation [m]
E	Energy [J]
F	Force [N]
h	Enthalpy [J/kg]
K	Bulk modulus [bar]
k	Scaling parameter [-]
Ma	Mach number [-]
m	Mass [kg]
$\vec{n}$	Free-surface unit normal [-]
Oh	Ohnesorge number [-]
P	Pressure [Pa]
Re	Reynolds number [-]
S	Surface area [m^2]
T	Temperature [K]
t	Time [s]
t_{shear}	Shear breakup timescale [s]
U, u	Velocity [m/s]
V	Volume [m^3]
v	Specific volume [m^3/kg]
ρ	Density [kg/m^3]
σ	Surface tension [N/m]
τ_r	Droplet relaxation time [s]
ϕ	Schlieren function [-]

Subscripts/Superscripts

*	Non-dimensional quantity
0	Initial
cm	Center of mass
cr	Cross-stream
d	Droplet
g	Gas
L	Liquid
mag	Magnitude
sh	Post-shock quantity
str	Streamwise
press	Pressure
ref	Reference
vol	Volumetric

Abbreviations

CLSVOF	Coupled Level-Set with VOF
DPM	Discrete phase model
EoS	Equation of state
KH	Kelvin-Helmholtz
LE	Leading-edge
LS	Level set

We	Weber number [-]	*RT*	Rayleigh-Taylor
Greek symbols		*RTP*	Rayleigh-Taylor piercing
α	Volume fraction [-]	*SIE*	Shear induced entrainment
ε	Density ratio [-]	*UDF*	User-defined function
μ	Dynamic viscosity [kg/(m·s)]	*VOF*	Volume of fluid

References

"ANSYS®FLUENT Theory Guide, 2014, Release 16.0."

Achenbach, E. 1974. "Vortex shedding from spheres." *Journal of Fluid Mechanics*, 62(02), 209-221.

Allaire, G., Clerc, S., and Kokh, S. 2002. "A five-equation model for the simulation of interfaces between compressible fluids." *Journal of Computational Physics*, 181(2), 577-616.

Barth, T., and Jespersen, D. 1989. "The design and application of upwind schemes on unstructured meshes." *Proc., 27th Aerospace sciences meeting*, 366.

Bo Shen, Q. Y., Oliver Tiedje, Joachim Domnick 2019. "Simulation of the primary breakup of non-Newtonian liquids at a high-speed rotary bell atomizer for spray painting processes using a VOF-Lagrangian Hybrid Model." *29th European Conference on Liquid Atomization and Spray Systems, ILASS*Paris.

Boiko, V., Papyrin, A., and Poplavskii, S. 1987. "Dynamics of droplet breakup in shock waves." *Journal of applied mechanics and technical physics*, 28(2), 263-269.

Boiko, V., and Poplavski, S. 2009. "On the dynamics of drop acceleration at the early stage of velocity relaxation in a shock wave." *Combustion, Explosion, and Shock Waves*, 45(2), 198-204.

Chang, C.-H., Deng, X., and Theofanous, T. G. 2013. "Direct numerical simulation of interfacial instabilities: a consistent, conservative, all-speed, sharp-interface method." *Journal of Computational Physics*, 242, 946-990.

Chang, C.-H., and Liou, M.-S. 2007. "A robust and accurate approach to computing compressible multiphase flow: Stratified flow model and AUSM+-up scheme." *Journal of Computational Physics*, 225(1), 840-873.

Engel, O. G. 1958. "Fragmentation of Waterdrops in the Zone Behind an Air Shock, J. Research Nat'i." *Bur. Stds*, 60(245), 19.

G. Strotos, I. M., N. Nikolopoulos, K. Papadopoulos, A. Theodorakakos, M.Gavaises. 2015. "Performance of VOF methodology in predicting the deformation and breakup of impulsively accelerated droplets." *ICLASS 2015, 13th Triennial International Conference on Liquid Atomization and Spray Systems, August 23-27*Tainan, Taiwan.

Gor, G. Y., Siderius, D. W., Shen, V. K., and Bernstein, N. 2016. "Modulus–pressure equation for confined fluids." *The Journal of chemical physics*, 145(16), 164505.

Green, B. 1995. *Fluid Vortices*, Springer Netherlands.

Guan, B., Liu, Y., Wen, C.-Y., and Shen, H. 2018. "Numerical Study on Liquid Droplet Internal Flow Under Shock Impact." *AIAA Journal*, 56(9), 3382-3387.

Guildenbecher, D. R., López-Rivera, C., and Sojka, P. E. 2009. "Secondary atomization." *Experiments in Fluids*, 46(3), 371-402.

Hébert, D., Rullier, J.-L., Chevalier, J.-M., Bertron, I., Lescoute, E., Virot, F., and El-Rabii, H. 2019. "Investigation of mechanisms leading to water drop breakup at Mach 4.4 and Weber numbers above 105." *SN Applied Sciences*, 2(1), 69.

Hirt, C. W., and Nichols, B. D. 1981. "Volume of fluid (VOF) method for the dynamics of free boundaries." *Journal of Computational Physics*, 39(1), 201-225.

Igra, D., and Takayama, K. 2001. "Numerical simulation of shock wave interaction with a water column." *Shock Waves*, 11(3), 219-228.

Igra, D., and Takayama, K. 2001. "A study of shock wave loading on a cylindrical water column." *Report of the Institute of Fluid Science, Tohoku University*, 13, 19-36.

Ivings, M., Causon, D., and Toro, E. 1998. "On Riemann solvers for compressible liquids." *International Journal for Numerical Methods in Fluids*, 28(3), 395-418.

Jain, S. S., Tyagi, N., Prakash, R. S., Ravikrishna, R., and Tomar, G. 2018. "Secondary breakup of drops at moderate Weber numbers: Effect of Density ratio and Reynolds number." *arXiv preprint arXiv:1803.02989*.

Johnsen, E. 2008. "Numerical simulations of non-spherical bubble collapse: With applications to shockwave lithotripsy." California Institute of Technology.

Joseph, D., Beavers, G., and Funada, T. 2002. "Rayleigh–Taylor instability of viscoelastic drops at high Weber numbers." *Journal of Fluid Mechanics*, 453, 109-132.
Joseph, D. D., Belanger, J., and Beavers, G. 1999. "Breakup of a liquid drop suddenly exposed to a high-speed airstream." *International Journal of Multiphase Flow*, 25(6-7), 1263-1303.
Kaiser, J., Adami, S., and Adams, N. A. 2017. "Direct Numerical Simulation of Shock-Induced Drop Breakup with a Sharp-Interface-Method." *Proc., Symposium on Turbulence and Shear Flow Phenomena [TSFP10]*.
Koukouvinis, P., Gavaises, M., Supponen, O., and Farhat, M. 2016. "Numerical simulation of a collapsing bubble subject to gravity." *Physics of Fluids*, 28(3), 032110.
Koukouvinis;, P., Roncero;, A. V., Rodriguez;, C., Gavaises;, M., and Picket, L. 2020. "High pressure/high temperature multiphase simulations of dodecane
injection to nitrogen: application on ECN Spray-A (under review)." *FUEL*.
Lafaurie, B., Nardone, C., Scardovelli, R., Zaleski, S., and Zanetti, G. 1994. "Modelling Merging and Fragmentation in Multiphase Flows with SURFER." *Journal of Computational Physics*, 113(1), 134-147.
Lemmon, E. 2013. "NIST Standard Reference Database 23, Reference Fluid Thermodynamic and Transport Properties (REFPROP), version 9.1, National Institute of Standards and Technology."
Liang, C. 2016. "Computational methods for the investigation of liquid drop phenomena in external gas flows." PhD Open Access Dissertation, Michigan Technological University.
Liou, M.-S., Chang, C.-H., Chen, H., and Hu, J.-J. 2009. "Numerical study of shock-driven deformation of interfaces." *Shock Waves*, Springer, 919-924.
Liu, N., Wang, Z., Sun, M., Wang, H., and Wang, B. 2018. "Numerical simulation of liquid droplet breakup in supersonic flows." *Acta Astronautica*, 145, 116-130.
Liu, Z., and Reitz, R. D. 1997. "An analysis of the distortion and breakup mechanisms of high speed liquid drops." *International Journal of Multiphase Flow*, 23(4), 631-650.
Malgarinos, I., Nikolopoulos, N., and Gavaises, M. 2015. "Coupling a local adaptive grid refinement technique with an interface sharpening scheme for the simulation of two-phase flow and free-surface flows using VOF methodology." *Journal of Computational Physics*, 300, 732-753.
Malgarinos, I., Nikolopoulos, N., and Gavaises, M. 2016. "A numerical study on droplet-particle collision dynamics." *International Journal of Heat and Fluid Flow*, 61, Part B, 499-509.
Malgarinos, I., Nikolopoulos, N., and Gavaises, M. 2017. "Numerical investigation of heavy fuel droplet-particle collisions in the injection zone of a Fluid Catalytic Cracking reactor, Part I: Numerical model and 2D simulations." *Fuel Processing Technology*, 156, 317-330.
Malgarinos, I., Nikolopoulos, N., and Gavaises, M. 2017. "Numerical investigation of heavy fuel droplet-particle collisions in the injection zone of a Fluid Catalytic Cracking reactor, part II: 3D simulations." *Fuel Processing Technology*, 156, 43-53.
Malgarinos, I., Nikolopoulos, N., Marengo, M., Antonini, C., and Gavaises, M. 2014. "VOF simulations of the contact angle dynamics during the drop spreading: Standard models and a new wetting force model." *Advances in Colloid and Interface Science*, 212, 1-20.
Meng, J., and Colonius, T. 2015. "Numerical simulations of the early stages of high-speed droplet breakup." *Shock Waves*, 25(4), 399-414.
Meng, J. C., and Colonius, T. 2018. "Numerical simulation of the aerobreakup of a water droplet." *Journal of Fluid Mechanics*, 835, 1108-1135.
Meng, J. C. C. 2016. "Numerical simulations of droplet aerobreakup." California Institute of Technology.
Menon, E. S. 2014. *Transmission pipeline calculations and simulations manual*, Gulf Professional Publishing.
Morsi, S., and Alexander, A. 1972. "An investigation of particle trajectories in two-phase flow systems." *Journal of Fluid Mechanics*, 55(2), 193-208.
Nicholls, J. A., and Ranger, A. A. 1969. "Aerodynamic shattering of liquid drops." *AIAA Journal*, 7(2), 285-290.
Perry, R. H., and Green, D. W. 1999. *Perry's Chemical Engineers' Handbook-Cdrom*, McGraw Hill.
Quirk, J. J., and Karni, S. 1996. "On the dynamics of a shock–bubble interaction." *Journal of Fluid Mechanics*, 318, 129-163.
Sakamoto, H., and Haniu, H. 1990. "A study on vortex shedding from spheres in a uniform flow." *ASME, Transactions, Journal of Fluids Engineering*, 112, 386-392.
Sonntag, R. E., Van Wylen, G. J., and Borgnakke, C. 2008. *Fundamentals of thermodynamics*, Wiley.
Stefanitsis, D., Malgarinos, I., Strotos, G., Nikolopoulos, N., Kakaras, E., and Gavaises, M. 2017. "Numerical investigation of the aerodynamic breakup of Diesel and heavy fuel oil droplets." *International Journal of Heat and Fluid Flow*, 68, 203-215.
Stefanitsis, D., Malgarinos, I., Strotos, G., Nikolopoulos, N., Kakaras, E., and Gavaises, M. 2017. "Numerical investigation of the aerodynamic breakup of Diesel droplets under various gas pressures." *28th Conference on Liquid Atomization and Spray Systems (ILASS-Europe 2017)*Valencia, Spain.
Stefanitsis, D., Malgarinos, I., Strotos, G., Nikolopoulos, N., Kakaras, E., and Gavaises, M. 2018. "Numerical investigation of the aerodynamic breakup of droplets in tandem." *International Journal of Multiphase Flow*.
Stefanitsis, D., Strotos, G., Nikolopoulos, N., and Gavaises, M. 2019. "Numerical investigation of the aerodynamic breakup of a parallel moving droplet cluster." *International Journal of Multiphase Flow*, 121, 103123.
Stefanitsis, D., Strotos, G., Nikolopoulos, N., Kakaras, E., and Gavaises, M. 2018. "Numerical examination of the aerodynamic breakup of droplets in chain formation." *14th Triennial International Conference on Liquid Atomization and Spray Systems (ICLASS 2018)*Chicago, USA.

618 Stefanitsis, D., Strotos, G., Nikolopoulos, N., Kakaras, E., and Gavaises, M. 2019. "Improved droplet breakup
619 models for spray applications." *International Journal of Heat and Fluid Flow*, 76, 274-286.
620 Strotos, G., Malgarinos, I., Nikolopoulos, N., and Gavaises, M. 2016. "Aerodynamic breakup of an n-decane droplet
621 in a high temperature gas environment." *Fuel*, 185, 370-380.
622 Strotos, G., Malgarinos, I., Nikolopoulos, N., and Gavaises, M. 2016. "Numerical investigation of aerodynamic
623 droplet breakup in a high temperature gas environment." *Fuel*, 181, 450-462.
624 Strotos, G., Malgarinos, I., Nikolopoulos, N., and Gavaises, M. 2016. "Predicting droplet deformation and breakup
625 for moderate Weber numbers." *International Journal of Multiphase Flow*, 85, 96-109.
626 Strotos, G., Malgarinos, I., Nikolopoulos, N., and Gavaises, M. 2016. "Predicting the evaporation rate of stationary
627 droplets with the VOF methodology for a wide range of ambient temperature conditions." *International*
628 *Journal of Thermal Sciences*, 109, 253-262.
629 Surov, V. 1995. "Numerical modeling of the interaction of a strong shock wave with liquid drops." *Journal of applied*
630 *mechanics and technical physics*, 36(3), 354-359.
631 Sutherland, W. 1893. "LII. The viscosity of gases and molecular force." *The London, Edinburgh, and Dublin*
632 *Philosophical Magazine and Journal of Science*, 36(223), 507-531.
633 Theofanous, T., and Li, G. 2008. "On the physics of aerobreakup." *Physics of Fluids*, 20(5), 052103.
634 Theofanous, T., Mitkin, V., Ng, C., Chang, C., Deng, X., and Sushchikh, S. 2012. "The physics of aerobreakup. II.
635 Viscous liquids." *Physics of Fluids*, 24(2), 022104.
636 Theofanous, T. G., Li, G. J., and Dinh, T. N. 2004. "Aerobreakup in Rarefied Supersonic Gas Flows." *Journal of*
637 *Fluids Engineering*, 126(4), 516-527.
638 Toro, E. F. 1997. "The Riemann Problem for the Euler Equations." *Riemann Solvers and Numerical Methods for*
639 *Fluid Dynamics: A Practical Introduction*, E. F. Toro, ed., Springer Berlin Heidelberg, Berlin, Heidelberg,
640 115-157.
641 Wagner, W., and Pruß, A. 2002. "The IAPWS formulation 1995 for the thermodynamic properties of ordinary water
642 substance for general and scientific use." *Journal of physical and chemical reference data*, 31(2), 387-
643 535.
644 Wierzba, A., and Takayama, K. 1988. "Experimental investigation of the aerodynamic breakup of liquid drops."
645 *AIAA Journal*, 26(11), 1329-1335.
646 Wu, J.-Z., Ma, H.-Y., and Zhou, M.-D. 2015. *Vortical Flows*, Springer-Verlag Berlin Heidelberg.
647 Xiao, F., Wang, Z., Sun, M., Liu, N., and Yang, X. 2017. "Simulation of drop deformation and breakup in supersonic
648 flow." *Proceedings of the Combustion Institute*, 36(2), 2417-2424.
649 Yi, X., Zhu, Y., and Yang, J. 2017. "On the Early-Stage Deformation of Liquid Drop in Shock-Induced Flow." *Proc.,*
650 *30th International Symposium on Shock Waves 2*, Springer, 1269-1273.
651 Yoshida, T., and Takayama, K. 1990. "Interaction of liquid droplets with planar shock waves." *Journal of Fluids*
652 *Engineering*, 112(4), 481-486.
653 Zandian, A., Sirignano, W. A., and Hussain, F. 2018. "Understanding liquid-jet atomization cascades via vortex
654 dynamics." *Journal of Fluid Mechanics*, 843, 293-354.
655

656 Table 1: Droplet diameter and non-dimensional numbers of the 2-D simulation of droplet breakup.

D_0 (m)	*We*	*Re*	*Oh*	ε	*Ma*
$4.8 \cdot 10^{-3}$	7355	107069	0.0017	831	1.47

657

658

659 Table 2: Droplet diameter and non-dimensional numbers of the 3-D simulation of droplet breakup.

D_0 (m)	*We*	*Re*	*Oh*	ε	*Ma*
$2.4 \cdot 10^{-3}$	780	191169	0.0024	617	1.24

660

661

List of figures

Figure 1: Computational domain utilized for the 2-D planar simulation of column breakup.

Figure 2: Computational domain utilized for the 3-D simulation of droplet breakup.

Figure 3: Pressure and Schlieren contours from the 2-D simulation of droplet breakup (α=0.5). Flow is from left to right.

Figure 4: a) Holographic interferograms from the experiment of (Igra and Takayama, 2001a) and numerical schlieren images from the simulations of b) (Meng and Colonius, 2015) and c) the current study, at two time instances. Flow is from left to right.

Figure 5: Temporal evolution of the non-dimensional a) streamwise deformation, b) cross-stream deformation and c) leading-edge displacement of the droplet, as predicted by the experiment of (Igra and Takayama, 2001a), the simulation of (Meng and Colonius, 2015) and the simulation of the current work (a=0.5).

Figure 6: Temporal evolution of droplet deformation as predicted by a) the experiment of (Theofanous et al., 2012), b) the simulation of (Meng and Colonius, 2018) (α=0.01) and c) the simulation of the current work (α=0.5). Flow is from left to right.

Figure 7: Contour in the X-Y plane (Z=0) of the non-dimensional pressure. Flow is from left to right.

Figure 8: Conical protuberance visible at the leading edge of the droplet (t^*=0.314).

Figure 9. Contribution of different vorticity generation mechanisms at a slice showing the droplet cross-section. (a) vortex stretching/tilting, (b) vortex dilation, (c) baroclinic torque, (d) viscous stresses and (e) body forces due to surface tension. All values are in the same units of vorticity generation rate (s-2). Note that the body force term actually contributes to dampen interfacial instabilities. The thick black line shows the droplet interface (volume fraction 0.5).

Figure 10: Temporal evolution of the dimensionless droplet a) velocity, b) displacement and c) acceleration, as well as d) the unsteady drag coefficient, as calculated in the current work and in the simulation of (Meng and Colonius, 2018).

687 Figure 11: Temporal evolution of droplet a) deformation in both axes (streamwise and cross-stream)

688 and b) surface area.

Click here to access/download;Figure;Figure 1.tif

Click here to access/download;Figure;Figure 2.tif

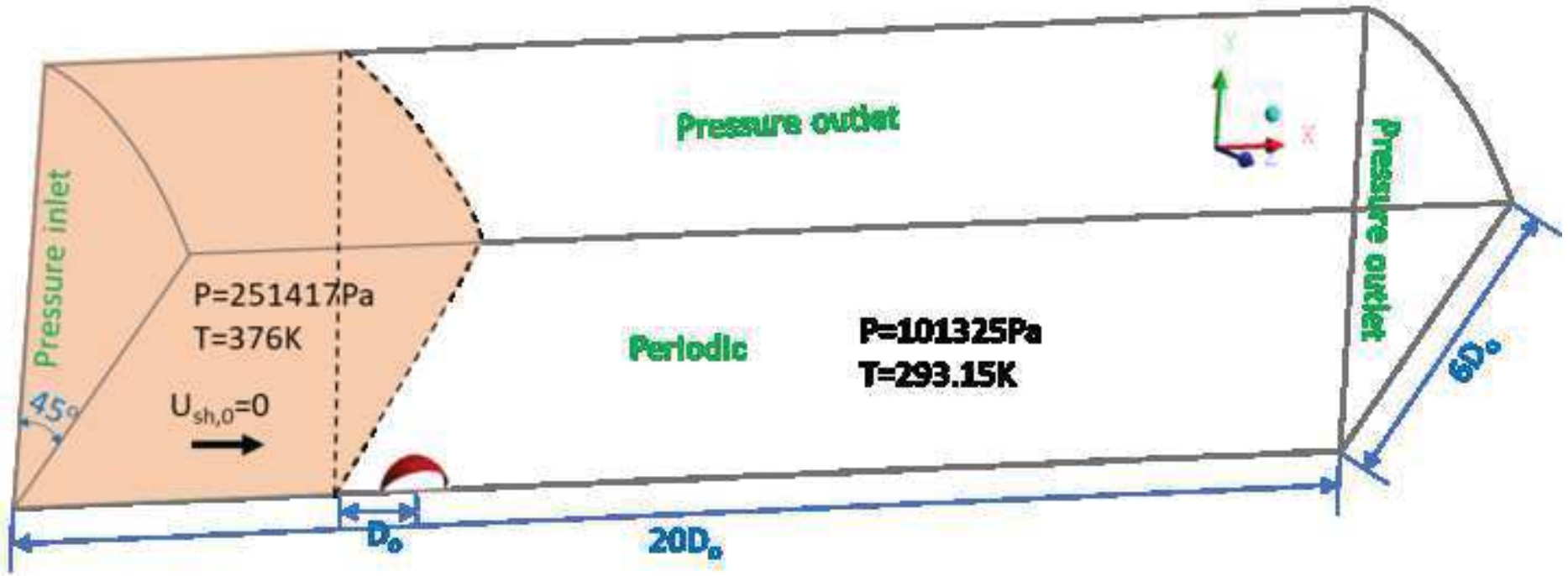

Click here to access/download;Figure;Figure 3.tif

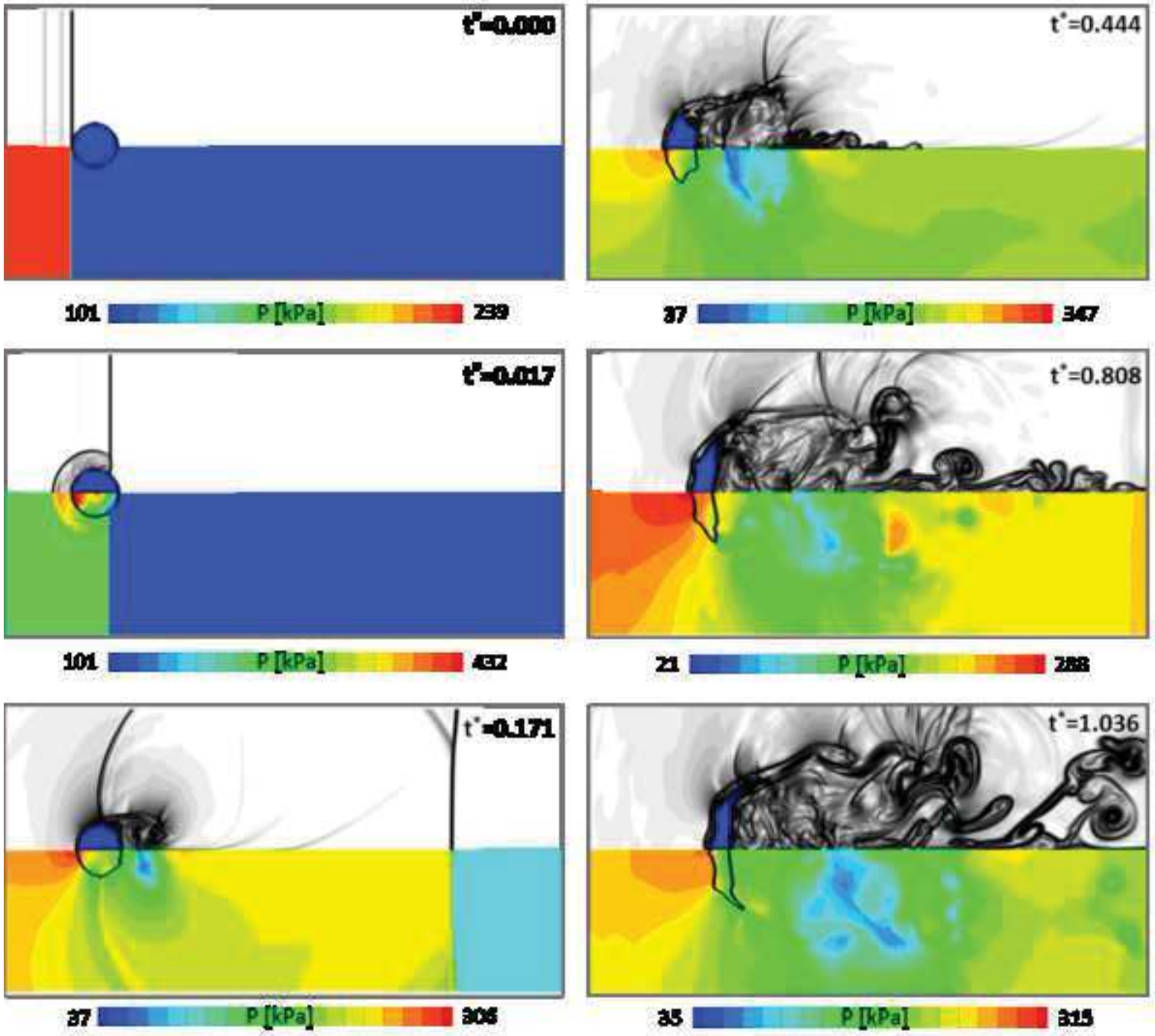

Click here to access/download;Figure;Figure 4.tif

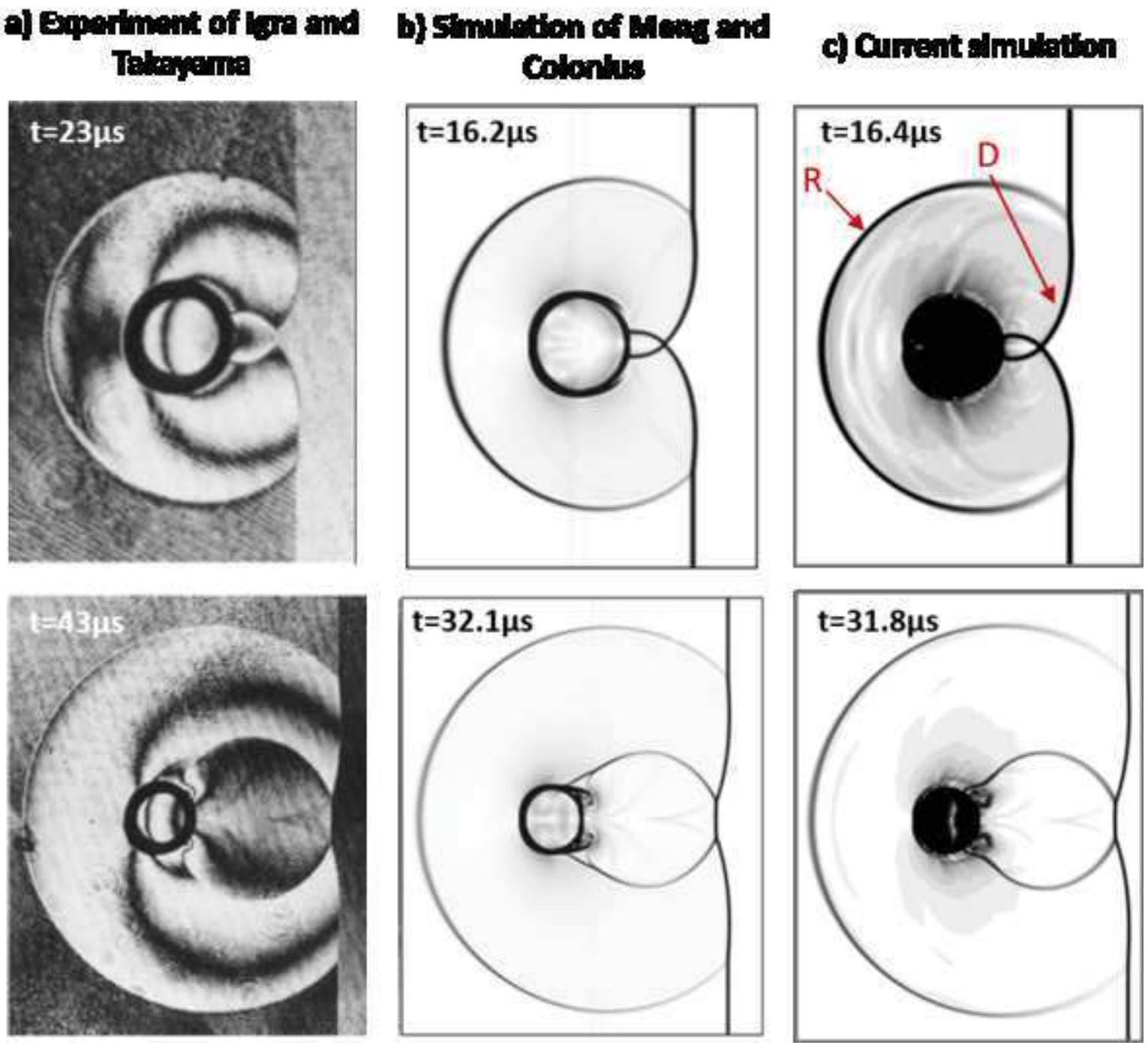

Click here to access/download;Figure;Figure 5.tif

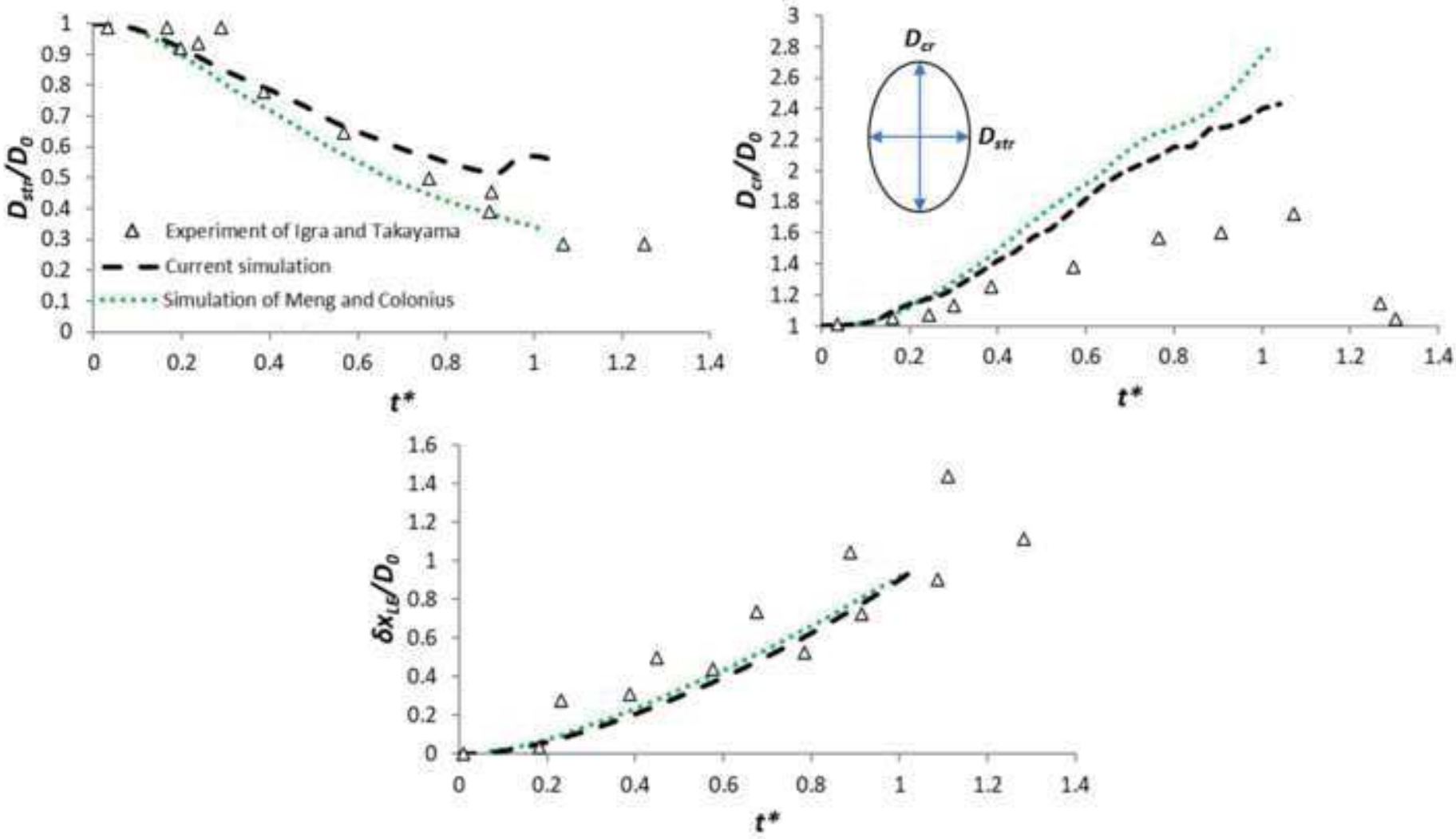

Click here to access/download;Figure;Figure 6.tif

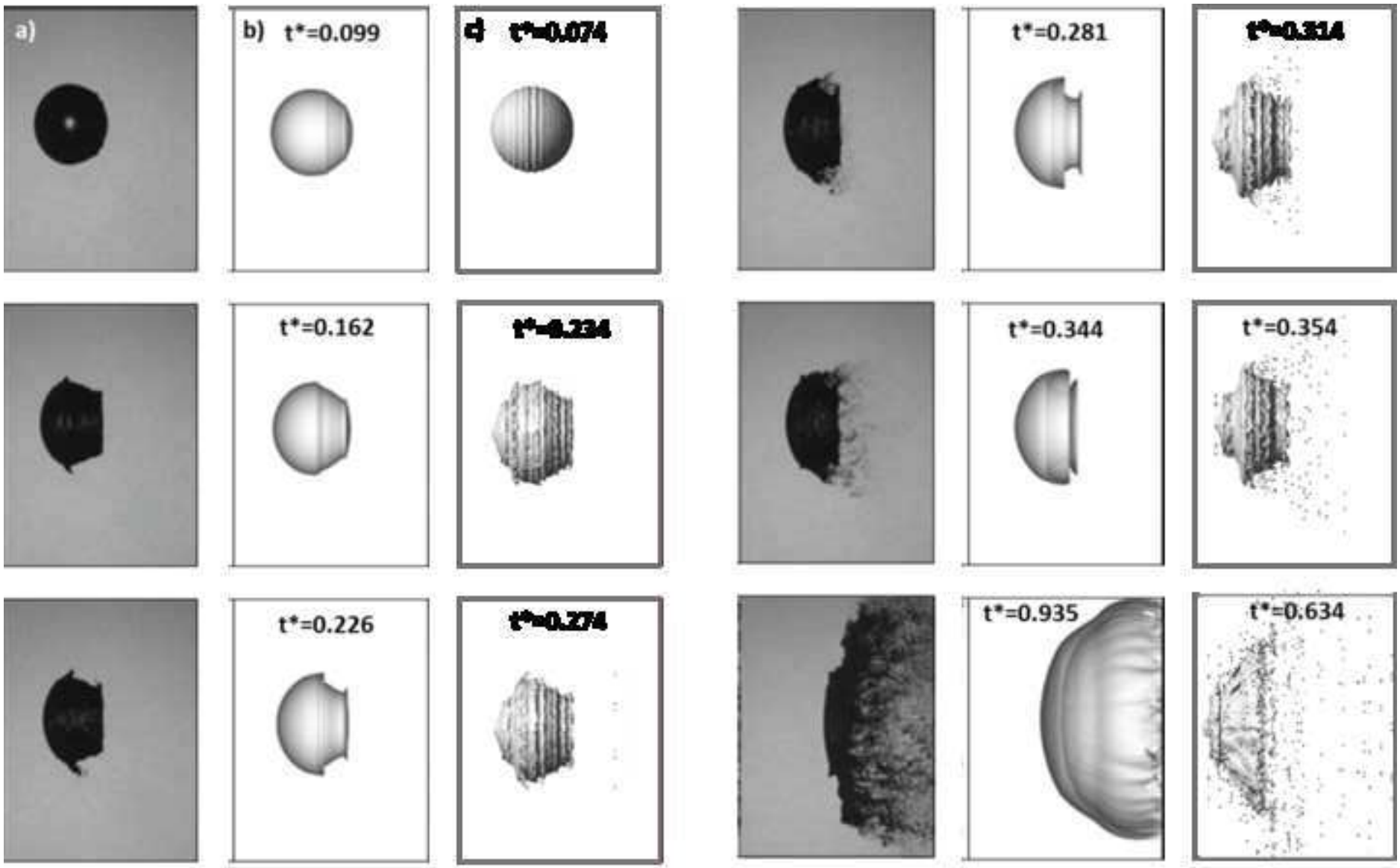

Click here to access/download;Figure;Figure 7.tif

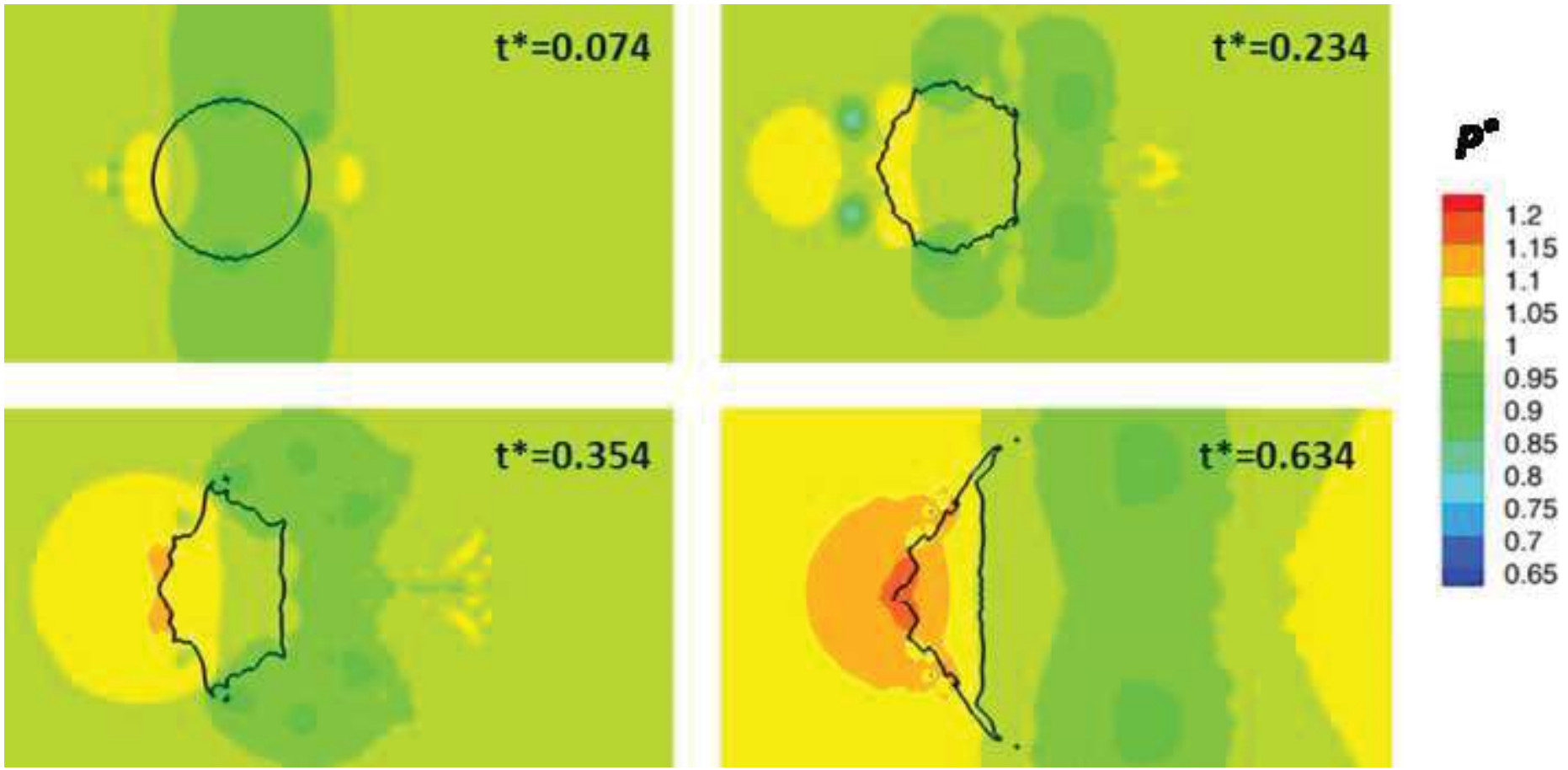

Click here to access/download;Figure;Figure 8.tif

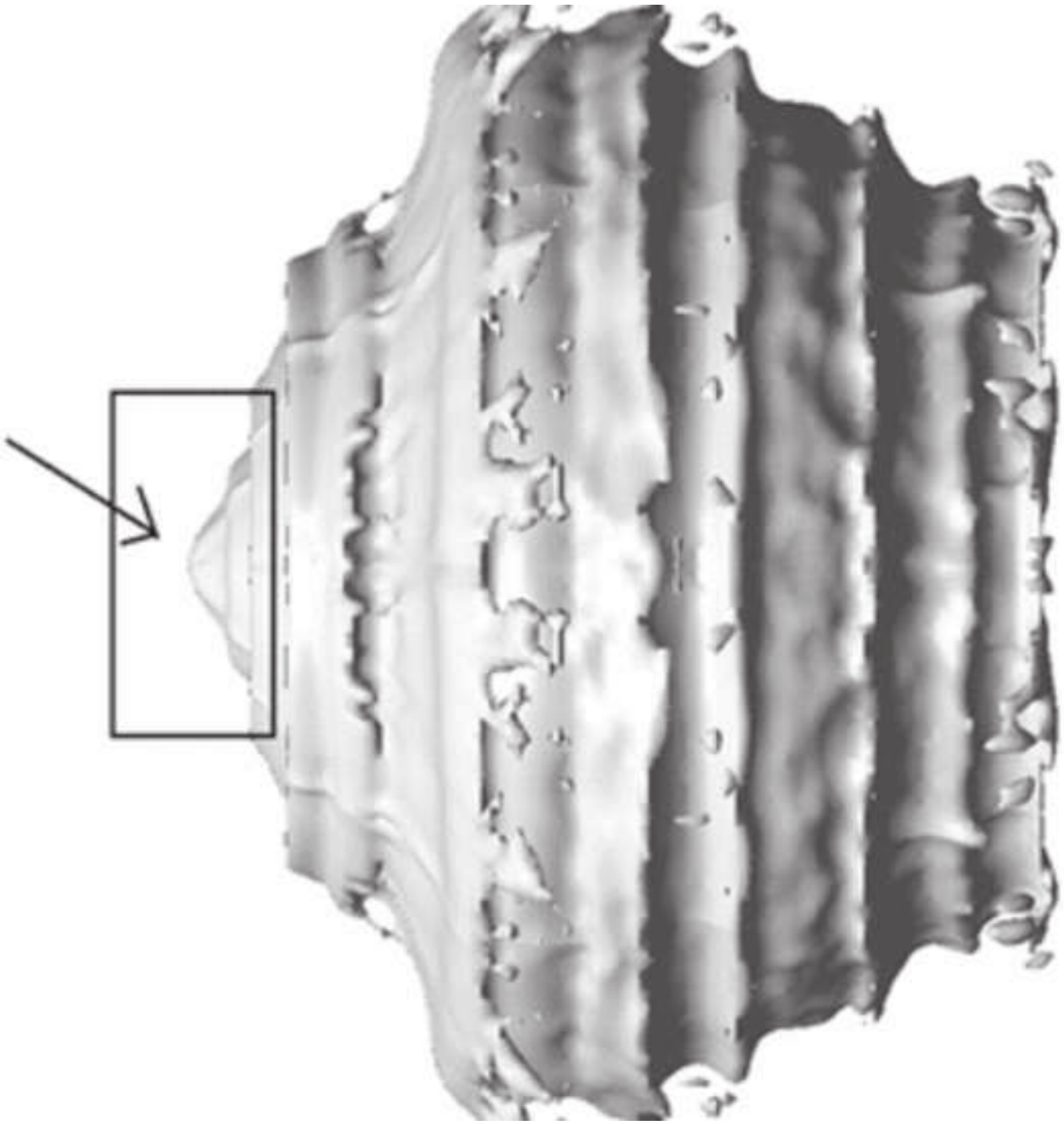

Click here to access/download;Figure;Figure 9.tif

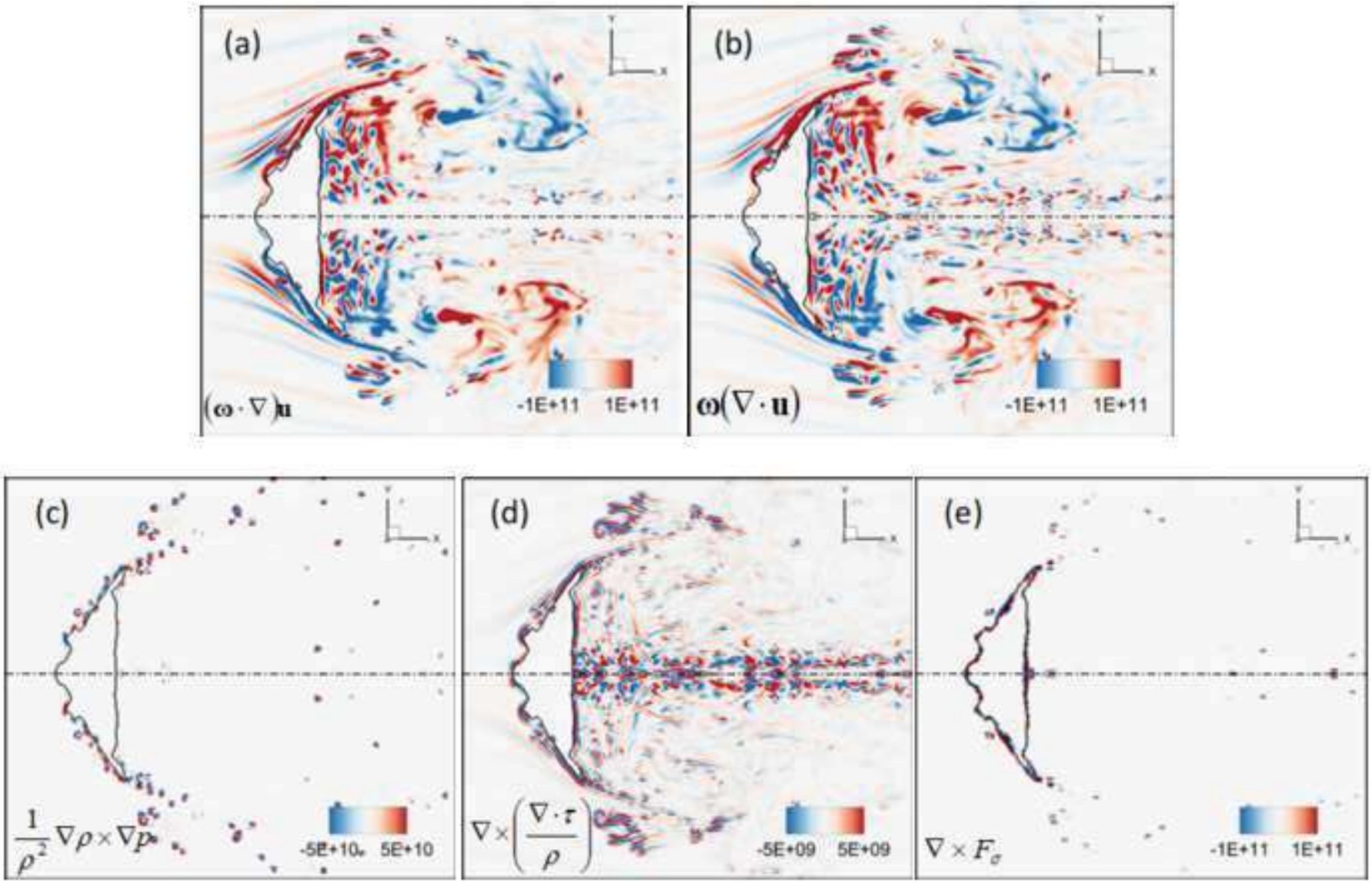

Click here to access/download;Figure;Figure 10.tif

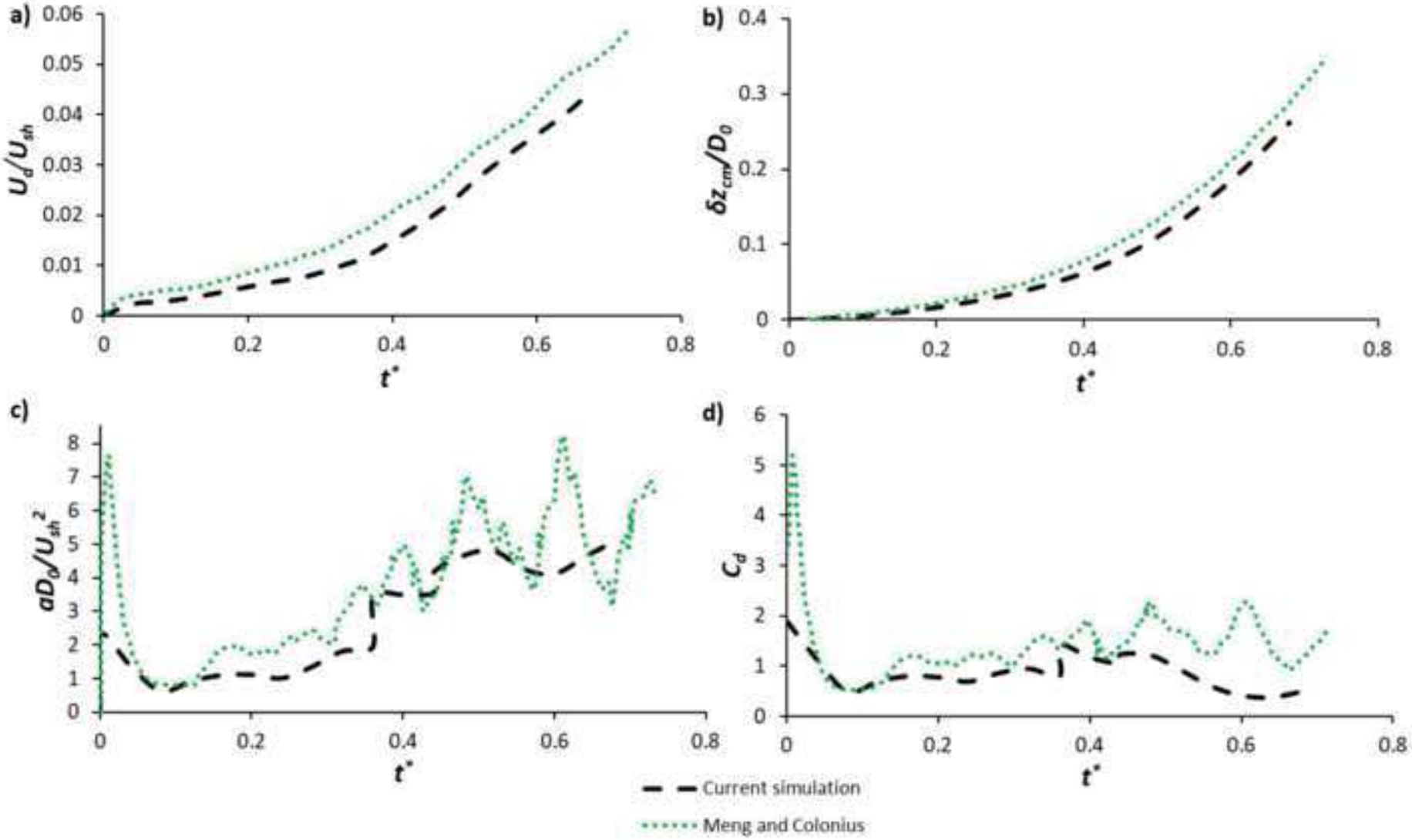
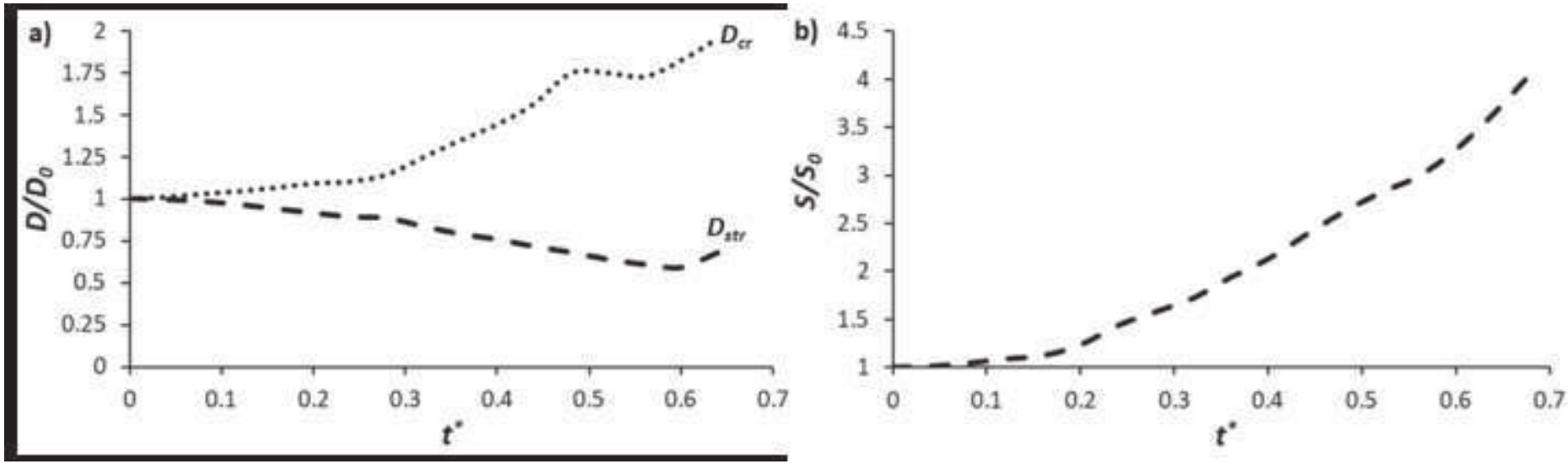
Click here to access/download;Figure;Figure 11.tif